

Performance-enhanced and cost-effective triboelectric nanogenerator based on stretchable electrode for wearable SpO₂ monitoring

Huamin Chen^{1,2}, Wei Yang¹, Cheng Zhang¹, Mingqiang Wu¹, Wenjie Li¹, Yuxiao Zou³, Longfeng Lv³, Hualiang Yu¹, Huizhen Ke⁷, Ruping Liu⁵, Yun Xu^{3,4}, Jun Wang¹ (✉), and Zhou Li^{2,6} (✉)

¹Fujian Key Laboratory of Functional Marine Sensing Materials, Center for Advanced Marine Materials and Smart Sensors, Minjiang University, Fuzhou 350108, China

²CAS Center for Excellence in Nanoscience, Beijing Key Laboratory of Micro-nano Energy and Sensor, Beijing Institute of Nanoenergy and Nanosystems, Chinese Academy of Sciences, Beijing 100083, China

³Institute of Semiconductors, Chinese Academy of Sciences, Beijing 100083, China

⁴Beijing Key Laboratory of Inorganic Stretchable and Flexible Information Technology, Beijing 100083, China

⁵Beijing Institute of Graphic Communication, Beijing 102600, China

⁶School of Nanoscience and Technology, University of Chinese Academy of Sciences, Beijing 100049, China

⁷Fujian Key Laboratory of Novel Functional Textile Fibers and Materials, Minjiang University, Fuzhou 350108, China

© Tsinghua University Press and Springer-Verlag GmbH Germany, part of Springer Nature 2021

Received: 30 May 2021 / Revised: 28 June 2021 / Accepted: 28 June 2021

ABSTRACT

Recently, stretchable and wearable health monitoring equipment has greatly improved human's daily life, which sets higher demands for portable power source in stretchability, sustainability, and biocompatibility. In this work, we proposed a stretchable triboelectric nanogenerator (TENG) based on stretchable poly (3,4-ethylenedioxythiophene):poly(styrenesulfonate) (PEDOT:PSS)/porous carbon hybrid for oxyhemoglobin saturation (SpO₂) monitoring. To combine advantages of carbon material for its high conductivity and organic electrode for its high stretchability, we spin-coated a solution of PEDOT:PSS/porous carbon onto a plasma-treated pre-stretched Ecoflex film to fabricate a stretchable electrode with rough surface. Due to its roughness and high potential difference with the dielectric material, the stretchable-electrode-based TENG exhibited better performance compared to the pristine TENG based on carbon or PEDOT:PSS material. The output voltage and current reached up to 51.5 V and 13.2 μ A as the carbon concentration increased. More importantly, the performance further increased under large strain (100%) which is suitable for wearable systems. Finally, the device demonstrated its application potential for powering a flexible blood oxygen monitor. This simple and cost-effective method can enhance the stretchability and stability of organic/inorganic electrode-based TENG, which paves the development of high-performance stretchable TENG.

KEYWORDS

triboelectric nanogenerator, stretchable, porous carbon, blood oxygen, poly (3,4-ethylenedioxythiophene):poly (styrenesulfonate) (PEDOT:PSS), wearable electronic

1 Introduction

Stretchable and wearable electronics has become a research hotspot in recent years for its great improvement to human's daily life, especially in health monitoring field. Diverse flexible sensors have emerged for electrophysiology and non-electrophysiology signal extraction such as blood oxygen and pulse [1–6]. However, the traditional power source such as battery cannot keep pace with the development of stretchable sensors. Wearable power source makes higher demands on stretchability, sustainability and biocompatibility, so as to improve the comfortability and practicality.

Triboelectric nanogenerator (TENG) originated from Maxwell's displacement current [7], is considered as the candidate for wearable power source for its outstanding characteristics including abundant materials [8–10], high output power [11–13], high cost-

effective [14–16], and desirable biocompatibility [17–19]. Since its birth in 2012 by Wang's group [20], great achievements have been made via various strategies such as materials optimization [21–23], structure design [24–28], charge pre-injection [29, 30], and environmental control [31–33]. Due to the great stretchability of organic insulating material, stretchable electrode design becomes the key constraints factors of high-performance stretchable TENG.

The simplest method to realize stretchable TENG is materials optimization. Various conductive liquid materials have been chosen to fabricate stretchable TENG such as water [34], hydrogel [35, 36], and liquid metal [37, 38], whose stretchability has broken through 2,500% [39]. However, it needs to improve the stability of the liquid materials to keep high performance. To reduce the effect of environment on the output performance, researchers proposed

stretchable electrode composed of conductive materials and elastomer [40–42]. Another common method is electrode structure design such as crumpled structure [43, 44], serpentine electrode [45] and fabric structure [46, 47]. Although many stretchable TENGs with high performance have been reported, the performance degradation under large strain is still a challenge, which impedes the development of stretchable power device.

In this work, we proposed a stretchable TENG based on crumpled poly(3,4-ethylenedioxythiophene):poly(styrenesulfonate) (PEDOT:PSS)/porous carbon for blood oxygen monitoring. We can obtain porous carbon by simply burning a candle [41]. Then we spin-coated a solution of PEDOT:PSS/porous carbon onto a pre-stretched Ecoflex film to fabricate a stretchable electrode. The TENG based on PEDOT:PSS/porous carbon showed better performance compared with PEDOT:PSS or porous carbon-based TENG. And its output voltage and current increased with increasing the carbon concentration. The output voltage and output current were 51.5 V and 13.2 μ A, respectively. More importantly, its output voltage and current enhanced to 74.3 V and 17.9 μ A when the device was under 100% strain. The enhancement of the output performance was attributed to the increased effective contact area. Finally, the stretchable TENG demonstrated its ability as a wearable power source by powering a flexible blood oxygen detector. This simple method can combine the advantages of stretchable organic electrode-based TENG and stable carbon-based TENG, which provides a novel strategy for robust stretchable TENG.

2 Experimental

2.1 The fabrication of stretchable TENG

Firstly, we put a clean glass sheet in the candle flame and moved the glass back and forth for about 40 s. The candle soot powder was deposited on the glass to form porous carbon. After scrapping the porous carbon, it was dispersed in PEDOT:PSS (1.5 wt.%) to form a PEDOT:PSS@porous carbon solution with various concentrations.

The Ecoflex (volume ratio of A:B = 1:1, 5 mL) was spin-coated on a silicon wafer at a speed of 200 rpm for 10 s and cured at 100 °C for 2 h. The thickness of the Ecoflex was 0.3 mm. Then it was treated by a plasma cleaner (Harrick plasma, PDC-002) to activate the surface of Ecoflex. The PEDOT:PSS@porous carbon of 3 mL was spin-coated onto the pre-stretched (150%) Ecoflex and cured at 90 °C for 1 h. After releasing the strain, PEDOT:PSS@porous carbon can form crumpled structure to realize a stretchable electrode. Compared to other stretchable materials, the Ecoflex possesses higher stretchability. As control groups, the porous carbon was directly deposited on the Ecoflex film, plasma-treated Ecoflex film and PEDOT:PSS/Ecoflex film, respectively.

The TENG was made of two separated films with a gap. The lower film was a stretchable electrode and the upper film was polytetrafluoroethylene (PTFE)/Au film or Ecoflex/PEDOT:PSS@porous carbon film. The two stretchable TENG films were connected and encapsulated by Ecoflex, which makes the device more stable.

2.2 The characterization of TENG

The surface morphology of the fabricated samples was characterized by a scanning electron microscope (SEM, SU8000), the Raman spectrum and the work function were measured by a spectrograph (Horiba HR Evolution 800) and self-built equipment. The porous carbon structure and the surface potential were conducted by the Brunauer–Emmett–Teller (BET) test and Kelvin probe force microscope (KPFM) test, respectively. The

roughness was characterized by the three-dimensional (3D) laser scanning microscope (VK-X200 series). The compressive force was applied by a linear mechanical motor, and the output voltage and current were measured by an oscilloscope (MDO 3000).

3 Results and discussion

The schematic structure of the fabricated TENG is illustrated in Fig. 1. As illustrated in Fig. 1(a), the device was made up of two functional films. The upper film consisted of PTFE triboelectric layer and gold electrode. The PTFE was strong electronegative and the nano-micro morphology can increase the triboelectric effect. The lower film was the crumpled porous carbon@PEDOT:PSS, which acted as the friction layer and the electrode. The two films were connected by four spacers. The fabrication process of the device is schematically exhibited in Fig. 1(b). The porous carbon was formed by the candle soot powder, and then the porous carbon was dispersed into PEDOT:PSS solution to form mixed solution with various concentrations. In order to enhance the surface hydrophilicity of stretchable Ecoflex, it was treated by a plasma cleaner. Finally, crumpled electrode was formed after releasing the pre-strain. The simple fabrication image of porous carbon is shown in Fig. 1(c). The SEM and Raman spectrum pictures of porous carbon are displayed in Figs. 1(d) and 1(e). The porous carbon on the silicon substrate in the Fig. 1(d) clearly showed the skeleton structure, which will improve its material activity. The Raman spectrum of the porous carbon is shown in Fig. 1(e). It displayed a sharpened G band and the I_D/I_G was 2.07. The BET measurement was also performed to prove the porous structure. The adsorption–desorption isotherm curve and aperture distribution curve are exhibited in Figs. 1(f) and 1(g). The average pore diameter was about 18 nm. The work function is also an important electronic property which greatly affects the output performance. We measured this parameter of porous carbon by our self-built equipment and the work function of 5.2 eV was obtained. And the standard KPFM testing of the electrodes was also conducted. The potential is about 0.2 V higher compared to the Au reference electrode.

The working principle of TENG is revealed in Fig. 2. The electron transfer process in the contact–separation mode is shown in Figs. 2(a)–2(e). In the initial state, the two films of the TENG were separated by the spacer. Under the force offered by the linear motor, the PTFE and porous carbon@PEDOT:PSS films tightly contacted, with the equal charges distributed on the two films. When releasing the force, the two films tended to separate. And the potential difference between the two electrodes drove the electrons to flow from the Cu electrode to the crumpled electrode. When the TENG returned to its initial state, the electrons nearly transferred to the Cu electrode. While pressing the device again, the potential difference drove the electrons to flow from the crumpled electrode to the Cu electrode. Then the two films tightly contacted again, and more charges should be distributed on the PTFE and crumpled electrode. In general, after several contact–separation processes, the charges on the PTFE will be saturated, and the output performance tends to be stable. In addition, the potential distribution on the open-circuit condition is shown in Figs. 2(f)–2(i) where the red color represents high potential and the blue color represents low potential. On the open-circuit condition, there was no electron transfer in the whole process. The potential difference between the two electrodes was proportional to the separation distance. The potential difference will reach the maximum value when the device returned to its initial state.

To investigate the electric properties of the TENG based on various crumpled electrodes, we constructed a series of TENGs

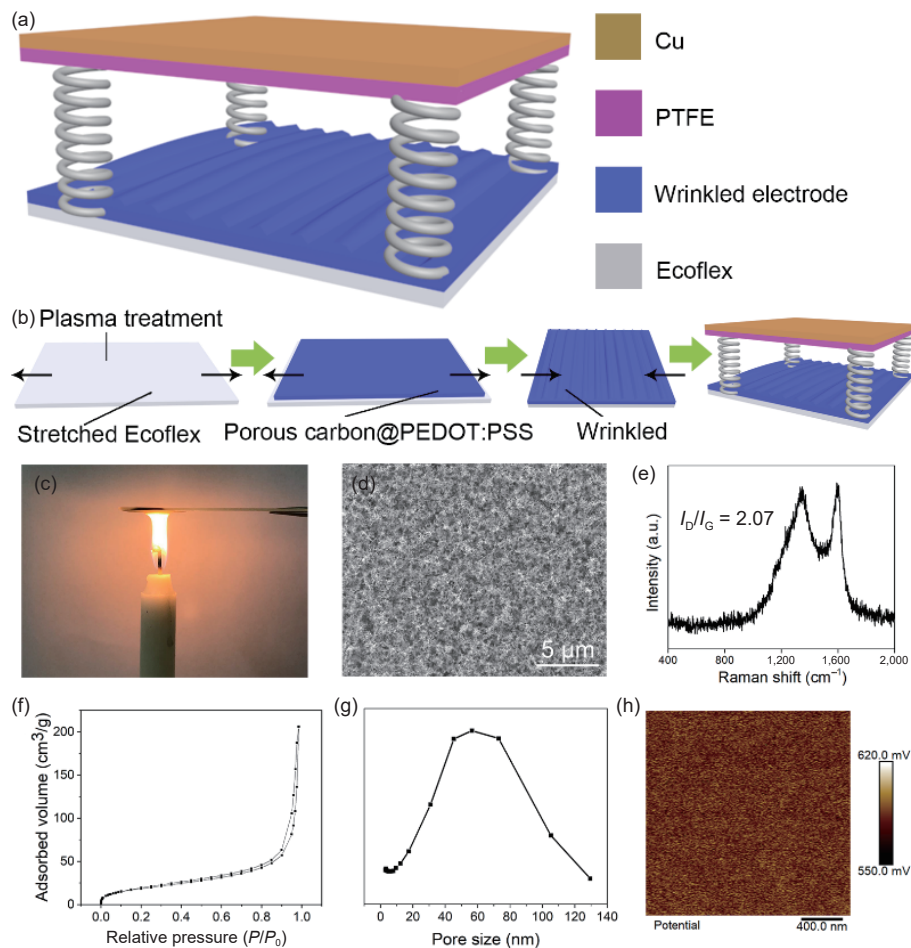


Figure 1 The device structure and materials properties of the fabricated TENG. (a) The schematic device structure of TENG. (b) The fabrication process of TENG. (c) The fabrication images of porous carbon. (d) The SEM picture of porous carbon. (e) The Raman spectrum image of porous carbon. (f) Testing of gas adsorption–desorption isotherm in the porous carbon. (g) The aperture distribution in the porous carbon. (h) The KPFM mapping of the PEDOT:PSS electrode.

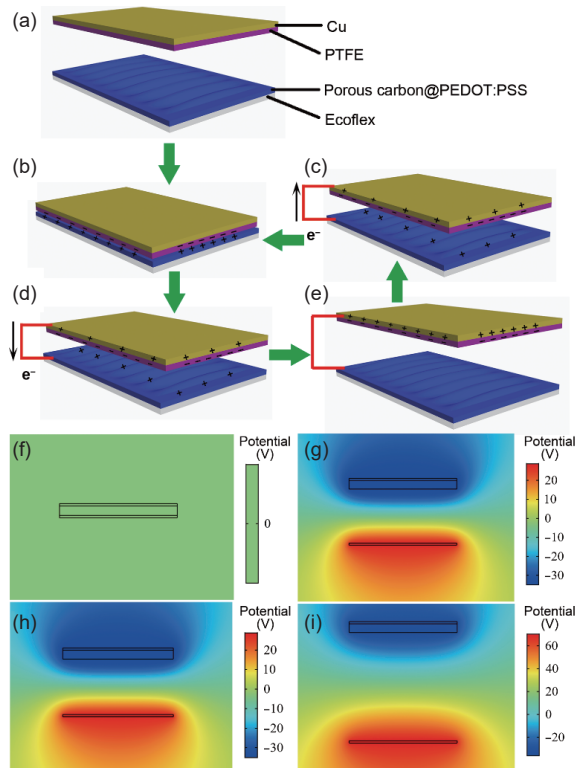


Figure 2 The working mechanism of TENG. (a)–(e) The electron transferring in the contact–separation process. (f)–(i) The calculated potential difference in the working process.

and characterized its output performance. The results are displayed in Fig. 3. The initial TENG was based on porous carbon without plasma treatment. And the other devices were treated by plasma, which was based on porous carbon, PEDOT:PSS, PEDOT:PSS/porous carbon, and porous carbon@PEDOT:PSS (2 mg/mL), respectively. In this experiment, the device structure was 1.5 cm², and the devices were pressed under 80 N at a frequency of 1 Hz. The output voltage of these devices based on various electrodes is shown in Fig. 3(a). The output voltage of the control group was 8.4 V. Although the porous carbon possesses high work function, it is not very compact layer. The porous carbon easily falls out during the triboelectric process. The output voltage of TENGs based on porous carbon, PEDOT:PSS, PEDOT:PSS/porous carbon, and porous carbon@PEDOT:PSS with plasma treatment was 10.2, 16.5, 17.6 and 19.9 V, respectively. The plasma treatment can activate the substrate to improve its surface adhesion. Therefore, the porous carbon was deposited more compactly which reduced the resistance of the electrode. The output voltage of the PEDOT:PSS based TENG was 16.5 V. The PEDOT:PSS was an ordinary organic electrode. However, the PEDOT:PSS solution cannot spread evenly on the Ecoflex substrate, and thus hydrophilic treatment of the stretchable substrate must be adopted to obtain uniform and compact thin film. The output voltage of TENG based on PEDOT:PSS/porous carbon electrode was 17.6 V, which showed a little improvement compared the PEDOT:PSS based TENG. On the one hand, the porous carbon deposited on the PEDOT:PSS film can improve its roughness and the potential difference with the PTFE, which will improve the output performance. On the

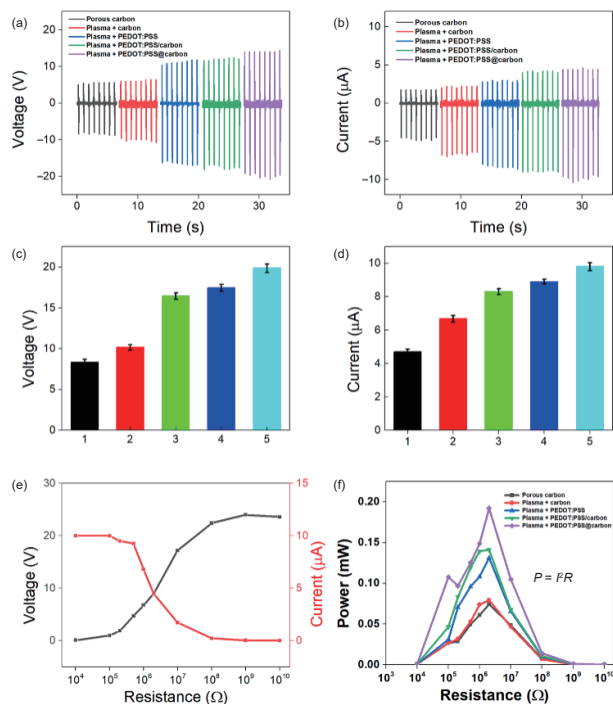


Figure 3 Electricity characterization of TENGs based on various electrodes. (a) The output voltage of TENGs based on various electrodes. (b) The output current of TENGs based on various electrodes. (c) The comparison of output voltage of various TENGs. (d) The comparison of output current of various TENGs. (e) The relationship of output voltage and output current with different load resistances. (f) The relationship between instantaneous output power of various TENGs and load resistances.

other hand, the porous carbon desquamation problem is more serious. The combination of the two effects resulted in a little enhancement in output voltage. In order to further utilize the strong electron donability of porous carbon to improve the output performance and stability, we mixed the porous carbon with the PEDOT:PSS solution to fabricate porous carbon@PEDOT:PSS electrode. Its output voltage was 19.9 V. The stretchable electrode was more stable because the carbon embedded in the PEDOT:PSS film. And the output voltage enhanced due to the higher potential difference between the triboelectric materials. The surface potential of the PEDOT:PSS and porous carbon@PEDOT:PSS was 0.584 and 0.557 V, respectively. The KPFM mapping of the two electrodes is shown in Fig. S1 in the Electronic Supplementary Material (ESM).

Meanwhile, the corresponding output current of these TENGs was 4.7, 6.7, 8.3, 8.9, and 9.8 μA , respectively, as shown in Fig. 3(b). The output current of these TENGs showed similar variation trend and the porous carbon@PEDOT:PSS based TENG showed the maximum output current. The histograms in Figs. 3(c) and 3(d) clearly displayed and compared the output voltage and output current. Then, the transferred charge of TENGs based on various electrodes was calculated according to the output current, as shown in Fig. S2 in the ESM. The transferred charge density was 19.2, 27.4, 33.1, 33.9, and 37.4 $\mu\text{C}/\text{m}^2$, respectively. The relationship of output performance with the load resistance is shown in Fig. 3(e). The change tendency of the output voltage and current with the load resistance in this experiment agrees well with the theoretical calculation (Chen et al., 2018). In addition, the output power of these devices is shown in Fig. 3(f). The output power of the control experiment was 0.07 mW under a corresponding resistance of 20 M Ω . And the output power of other devices was 0.08, 1.31, 1.41, and 1.92 mW, respectively. The output power of porous carbon@PEDOT:PSS based TENG showed about 27-fold improvement. As an important figure of

merit, the average power density (W) was obtained by the following equation

$$W = \frac{\int_{T_1}^{T_2} FRdt}{S(T_2 - T_1)} = 0.31 \text{ mW}/\text{cm}^2 \quad (1)$$

where the time span between T_2 and T_1 represents a single cycle, R is the load resistance and S is the contact area.

To further demonstrate the effect of the porous carbon on the output performance, we measured the output performance of TENG based on porous carbon@PEDOT:PSS with various concentrations. The devices were compressed under a force of 100 N at a frequency of 1 Hz, and the results are shown in Fig. 4. As shown in Fig. 4(a), the output voltages of these devices were 33.1 V (2 mg/mL), 36.2 V (4 mg/mL), 37.3 V (6 mg/mL), 37.9 V (8 mg/mL), and 51.5 V (10 mg/mL), respectively. It was clear that the output voltage enhanced with the concentration increasing. Significantly, the output voltage of the TENG with various concentrations (4, 6, and 8 mg/mL) showed a tiny difference. So the output voltage greatly enhanced when the concentration reached up to 10 mg/mL. The corresponding output currents shown in Fig. 4(b) were 8.1, 10.9, 11.2, 11.5, and 13.2 μA , respectively, which revealed the same trend. And the corresponding transferred charge is shown in Fig. S3 in the ESM. The enhancement is mainly due to the increase of roughness caused by the porous carbon. As shown in Fig. S4 in the ESM, the surface roughness was increased from 4.8 to 8.2 μm as the concentration increased from 2 to 10 mg/mL. The increased surface roughness can enhance the contact area between the electrode and the PTFE film, which is favor of the increase of output power. In addition, we investigated the relationship between the output performance and the frequency. The porous carbon@PEDOT:PSS based TENG (6 mg/mL) was pressed under a force of 100 N. The output voltage of TENG in Fig. 4(c) increased from 37.2 to 53.6 V as the frequency increased from 0.17 to 1.33 Hz, and then it decreased to 40.8 V as the frequency further increased to 1.67 Hz. And the output current in Fig. 4(d) showed the similar trend. The output current of the TENG enhanced from 9.47 to 15.7 μA , and then reduced to 11.0 μA . The performance enhancement is mainly on account of higher electron transfer. Normally, the performance can further increase as the frequency further increases. The decrease may be caused by the equipment limitation. In the high frequency motion, the moving itinerary of the motor will decrease, resulting in inadequate contact between the two films.

The output performance of the stretchable TENG under stretching state is another important parameter. The porous carbon@PEDOT:PSS based TENG (10 mg/mL) was compressed under a force of 100 N at the frequency of 1.33 Hz, and the measured results are shown in Fig. 5. As shown in Fig. 5(a), the output voltage of the device in the initial state was 48.6 V. And then, the length of the stretchable electrode was stretched from 1.5 to 3 cm, which was twice the original length. The output voltage of the TENG under stretched state was 74.3 V. And the output current of the device under initial state and stretching state was 12.8 and 17.9 μA , as shown in Fig. 5(b). The relationship between the output voltage and the strain is shown in Fig. 5(c). As the strain increased from 0% to 100%, the output voltage rapidly increased. And when the strain exceeded 100%, the resistance of the stretchable electrode largely increased, which resulted in the rapidly decrease of device performance. The relationship between the output current and the strain showed the similar trend, as shown in Fig. S5 in the ESM. And the cyclic stretching test is exhibited in Fig. 5(d). The output performance retained stable after about 5,000 stretching cycles, confirming the long-term

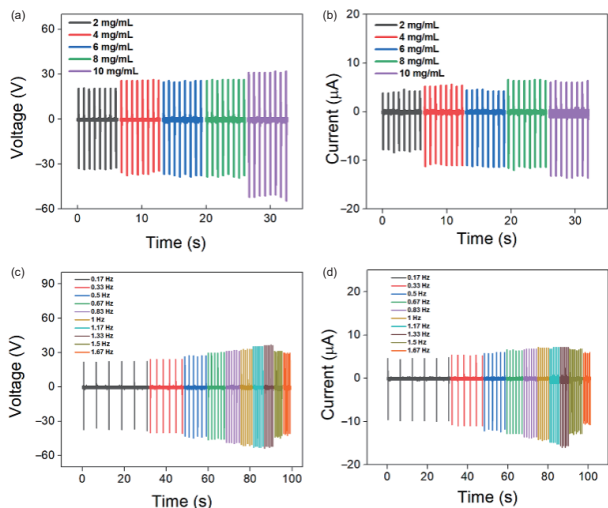


Figure 4 The effect of the concentration and pressing frequency on the output performance. (a) The output voltage of TENG based on porous carbon@PEDOT:PSS with various concentrations. (b) The output current of TENG based on porous carbon@PEDOT:PSS with various concentrations. (c) The relationship between the output voltage and pressing frequency. (d) The relationship between the output current and pressing frequency.

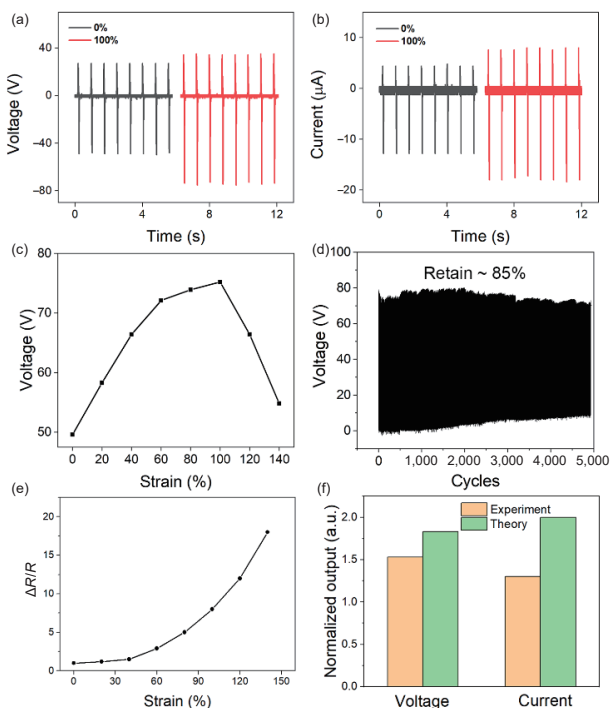


Figure 5 The comparison of the output performance of TENG under initial state and stretching state. (a) The output voltage of TENG under initial state and stretching state. (b) The output current of TENG under initial state and stretching state. (c) The relationship between the output performance and the strain. (d) The cyclic stretching tests for the stretchable TENG. (e) The relationship between the resistance variation and the strain. (f) The calculated output performance and the measured output performance.

durability of the device. The output performance of the TENG under stretching state showed a great enhancement which was the result of resistance and effective contact area variation. The relationship between the resistance variation and the strain is revealed in Fig. 5(e). The resistance–strain curve showed that the resistance increased slowly as the strain increased, and then increased rapidly under large strain. Under small strain, the crumpled electrode unfolds and forms new conductive channel, so the resistance change is small. Under large strain, the crumpled electrode further unfolds, and cracks perpendicular to the strain

direction will appear, which results in the rapid increase of resistance. The larger resistance has a negative effect on the output performance. Then we calculated the relationship between the output performance and the effective contact area. The comparison of the experimental performance and the calculated result is shown in Fig. 5(f). The initial area and the stretched area were 1.5 and 3 cm², respectively. According to our previous work, the transferred charges can be calculated as follows

$$Q(t) = \exp\left(-\frac{6md_0t + (F - mg)t^3}{6mRSE_0}\right) \times \int_0^t \frac{\sigma(F - mg)t^2}{2mRE_0} \exp\left(\frac{6md_0t + (F - mg)t^3}{6mRSE_0}\right) dt \quad (2)$$

where ϵ_0 , ϵ_r , and σ are the vacuum permittivity, relative permittivity, and the surface charge density, respectively; F , m , S , d_0 , R are the force, the mass, effective area, thickness of dielectric layer, and load resistance, respectively.

From the normalized results, we can see that the numerical voltage and current were higher than our experimental results. This is mainly due to the increased resistance of triboelectric electrode. The increased resistance will reduce the transfer speed of electrons, thus decreasing the output performance.

The charge ability of the TENG is a key parameter to evaluate its potential to be a power source. The alternating current (AC) output performance of the TENG was rectified to power a capacitor, as shown in Fig. 6(a). The voltage of the capacitor was measured by an oscilloscope. The TENG was pressed under a force of 50 N at a frequency of 1 Hz. As exhibited in Fig. 6(b), various capacitors (1, 2.2, 4.7, and 10 μ F) were charged in 60 s. A capacitor of 1 μ F was charged to about 3 V in 30 s. And even the capacitor of 10 μ F can be charged to more than 1 V in 60 s. It demonstrated the ability to charge energy storage unit. Furthermore, its stability test is characterized in Fig. 6(c). The output voltage was stable about 60 V after 1,000 cycles. There was nearly no degradation of output performance. Afterward, 29 commercial red light-emitting diodes (LEDs) arranged a pattern of MJU, which was instantaneously lit up by pressing the TENG by a finger. The photographs of lighted LEDs in the dark are shown in Fig. 6(d).

Based on its charge ability, the device was demonstrated to form a self-powered system for monitoring the blood oxygen. The structure diagram and the measurement principle are illustrated in Fig. 7(a). The flexible blood oxygen detector was made up of two

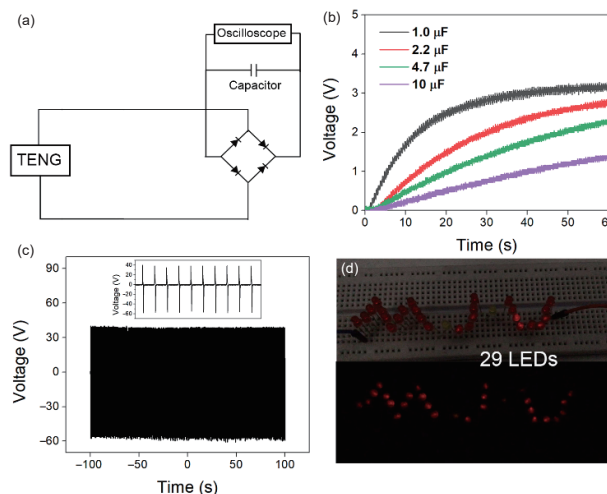


Figure 6 The charge ability of the TENG. (a) The schematic charge circuit. (b) The charge curve of various capacitors in 60 s. (c) The stability test of the TENG. (d) The LEDs powered by the TENG.

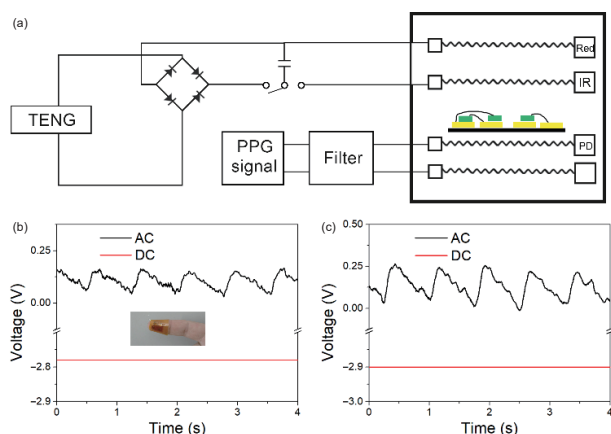


Figure 7 The self-powered flexible blood oxygen monitoring system based on TENG. (a) The structure diagram of the system. (b) The PPG signal measured by the red LED. (c) The PPG signal measured by the infrared LED.

LEDs and a photodetector (PD), which was connected by the serpentine wire. The small black squares represent the electrode pad, which can reduce the contact resistance of the electrode lead. By mounting the flexible device on the finger pulp, the Si detector can receive the light signal, which can be converted into photoplethysmography (PPG) signal by a filter (Stanford Research System SR640) and an oscilloscope. The wavelength of the red LED and infrared (IR) LED were 647 and 858 nm, respectively. The LEDs were powered by a supercapacitor charged by the TENG. The measured PPG signals are shown in Figs. 7(b) and 7(c). The PPG signal measured by the red LED is displayed in Fig. 7(b). The inset picture is the flexible blood oxygen monitor tightly attached to the finger pulp. In the AC and direct current (DC) coupled mode, we can obtain a PPG signal and a straight line, respectively. Likewise, we can measure two lines by infrared LED, as shown in Fig. 7(c). According to the Lambert–Beer law, the oxyhemoglobin saturation (SpO_2) can be derived from the four curves [48]. The self-powered blood oxygen detector can sustainably and stably measure the physiological signal, which provides the potential for battery-free wearable electronics.

4 Conclusions

In summary, we proposed a self-powered flexible blood oxygen monitor powered by stretchable TENG based on crumpled PEDOT:PSS/porous carbon. We can fabricate abundant porous carbon by simply burning a candle. Then we spin-coated a solution of PEDOT:PSS/porous carbon onto a plasma-treated pre-stretched Ecoflex film to fabricate a stretchable electrode. Due to its strong electron donability and conductivity, the PEDOT:PSS/porous carbon-based TENG revealed better performance compared to PEDOT:PSS or porous carbon-based TENG. And its output performance enhanced with increasing the carbon concentration. More importantly, its output voltage and current enhanced to 74.3 V and 17.9 μ A when the device was under 100% strain. The enhancement of the output performance was attributed to the increased effective contact area. So the device performance will not degrade under stretchable work environment. Finally, the stretchable TENG demonstrated the application potential for powering a flexible blood oxygen detector. This simple and economical method can enhance the electrical properties of organic electrode-based TENG and the stability of carbon-based TENG, which paves the development of high-performance stretchable TENG.

Acknowledgements

This work was supported by the National Natural Science Foundation of China (Nos. 11674185, 61875015, and 61971049), the Natural Science Foundation of Fujian (Nos. 2020J01857 and 2019J01764), the Fuzhou City Science and Technology Cooperation Project (Nos. 2020-GX-5 and 2020-S-29), Beijing Natural Science Foundation (No. JQ20038), the Key Scientific Research Project of Beijing Municipal Commission of Education (No. KZ202010015024), the Research and Development Program of Beijing Institute of Graphic Communication (No. Ec202006), and the Beijing Municipal Science and Technology Commission (No. Z181100004418004).

Electronic Supplementary Material: Supplementary material (KPFM measurements, the calculated transferred charge and the surface roughness measurement) is available in the online version of this article at <https://doi.org/10.1007/s12274-021-3724-1>.

References

- Chen, Y.; Zhang, Y. C.; Liang, Z. W.; Cao, Y.; Han, Z. Y.; Feng, X. Flexible inorganic bioelectronics. *npj Flex. Electron.* **2020**, *4*, 2.
- Li, H. C.; Ma, Y. J.; Liang, Z. W.; Wang, Z. H.; Cao, Y.; Xu, Y.; Zhou, H.; Lu, B. W.; Chen, Y.; Han, Z. Y. et al. Wearable skin-like optoelectronic systems with suppression of motion artifacts for cuffless continuous blood pressure monitor. *Natl. Sci. Rev.* **2020**, *7*, 849–862.
- Kim, J.; Gutruf, P.; Chiarelli, A. M.; Heo, S. Y.; Cho, K.; Xie, Z. Q.; Banks, A.; Han, S.; Jang, K. I.; Lee, J. W. et al. Miniaturized battery-free wireless systems for wearable pulse oximetry. *Adv. Funct. Mater.* **2017**, *27*, 1604373.
- Kim, J.; Salvatore, G. A.; Araki, H.; Chiarelli, A. M.; Xie, Z. Q.; Banks, A.; Sheng, X.; Liu, Y. H.; Lee, J. W.; Jang, K. I. et al. Battery-free, stretchable optoelectronic systems for wireless optical characterization of the skin. *Sci. Adv.* **2016**, *2*, e1600418.
- Kim, D. H.; Lu, N. S.; Ma, R.; Kim, Y. S.; Kim, R. H.; Wang, S. D.; Wu, J.; Won, S. M.; Tao, H.; Islam, A. et al. Epidermal electronics. *Science* **2011**, *333*, 838–843.
- Li, H. B.; Lv, S. Y.; Fang, Y. Bio-inspired micro/nanostructures for flexible and stretchable electronics. *Nano Res.* **2020**, *13*, 1244–1252.
- Wang, Z. L. On Maxwell's displacement current for energy and sensors: The origin of nanogenerators. *Mater. Today* **2017**, *20*, 74–82.
- Li, S. Y.; Nie, J. H.; Shi, Y. X.; Tao, X. L.; Wang, F.; Tian, J. W.; Lin, S. Q.; Chen, X. Y.; Wang, Z. L. Contributions of different functional groups to contact electrification of polymers. *Adv. Mater.* **2020**, *32*, 2001307.
- Zou, H. Y.; Zhang, Y.; Guo, L. T.; Wang, P. H.; He, X.; Dai, G. Z.; Zheng, H. W.; Chen, C. Y.; Wang, A. C.; Xu, C. et al. Quantifying the triboelectric series. *Nat. Commun.* **2019**, *10*, 1427.
- Fan, F. R.; Lin, L.; Zhu, G.; Wu, W. Z.; Zhang, R.; Wang, Z. L. Transparent triboelectric nanogenerators and self-powered pressure sensors based on micropatterned plastic films. *Nano Lett.* **2012**, *12*, 3109–3114.
- Lim, K. W.; Peddigari, M.; Park, C. H.; Lee, H. Y.; Min, Y.; Kim, J. W.; Ahn, C. W.; Choi, J. J.; Hahn, B. D.; Choi, J. H. et al. A high output magneto-mechano-triboelectric generator enabled by accelerated water-soluble Nano-bullets for powering a wireless indoor positioning system. *Energy Environ. Sci.* **2019**, *12*, 666–674.
- Xie, Y. N.; Wang, S. H.; Niu, S. M.; Lin, L.; Jing, Q. S.; Yang, J.; Wu, Z. Y.; Wang, Z. L. Grating-structured freestanding triboelectric-layer nanogenerator for harvesting mechanical energy at 85% total conversion efficiency. *Adv. Mater.* **2014**, *26*, 6599–6607.
- Zhao, P. F.; Bhattacharya, G.; Fishlock, S. J.; Guy, J. G. M.; Kumar, A.; Tsonos, C.; Yu, Z. D.; Raj, S.; McLaughlin, J. A.; Luo, J. K. et al. Replacing the metal electrodes in triboelectric nanogenerators: High-performance laser-induced graphene electrodes. *Nano Energy* **2020**, *75*, 104958.
- Peng, F.; Liu, D.; Zhao, W.; Zheng, G. Q.; Ji, Y. X.; Dai, K.; Mi, L. W.; Zhang, D. B.; Liu, C. T.; Shen, C. Y. Facile fabrication of

- triboelectric nanogenerator based on low-cost thermoplastic polymeric fabrics for large-area energy harvesting and self-powered sensing. *Nano Energy* **2019**, *65*, 104068.
- [15] Zhong, Q. Z.; Zhong, J. W.; Hu, B.; Hu, Q. Y.; Zhou, J.; Wang, Z. L. A paper-based nanogenerator as a power source and active sensor. *Energy Environ. Sci.* **2013**, *6*, 1779–1784.
- [16] Xia, K. Q.; Xu, Z. W.; Zhu, Z. Y.; Zhang, H. Z.; Nie, Y. Cost-effective copper–nickel-based triboelectric nanogenerator for corrosion-resistant and high-output self-powered wearable electronic systems. *Nanomaterials* **2019**, *9*, 700.
- [17] Chen, H. M.; Bai, L.; Li, T.; Zhao, C.; Zhang, J. S.; Zhang, N.; Song, G. F.; Gan, Q. Q.; Xu, Y. Wearable and robust triboelectric nanogenerator based on crumpled gold films. *Nano Energy* **2018**, *46*, 73–80.
- [18] Chen, H. M.; Xu, Y.; Bai, L.; Jiang, Y.; Zhang, J. S.; Zhao, C.; Li, T.; Yu, H. L.; Song, G. F.; Zhang, N. et al. Crumpled graphene triboelectric nanogenerators: Smaller devices with higher output performance. *Adv. Mater. Technol.* **2017**, *2*, 1700044.
- [19] Fan, F. R.; Tian, Z. Q.; Wang, Z. L. Flexible triboelectric generator. *Nano Energy* **2012**, *1*, 328–334.
- [20] Seol, M.; Kim, S.; Cho, Y.; Byun, K. E.; Kim, H.; Kim, J.; Kim, S. K.; Kim, S. W.; Shin, H. J.; Park, S. Triboelectric series of 2D layered materials. *Adv. Mater.* **2018**, *30*, 1801210.
- [21] Chen, H. M.; Xu, Y.; Zhang, J. S.; Wu, W. T.; Song, G. F. Enhanced stretchable graphene-based triboelectric nanogenerator via control of surface nanostructure. *Nano Energy* **2019**, *58*, 304–311.
- [22] Zhu, G.; Chen, J.; Zhang, T. J.; Jing, Q. S.; Wang, Z. L. Radial-arrayed rotary electrification for high performance triboelectric generator. *Nat. Commun.* **2014**, *5*, 3426.
- [23] Gao, Y. Y.; Liu, G. X.; Bu, T. Z.; Liu, Y. Y.; Qi, Y. C.; Xie, Y. T.; Xu, S. H.; Deng, W. L.; Yang, W. Q.; Zhang, C. MXene based mechanically and electrically enhanced film for triboelectric nanogenerator. *Nano Res.*, in press, DOI: [10.1007/s12274-021-3437-5](https://doi.org/10.1007/s12274-021-3437-5).
- [24] Chun, J.; Ye, B. U.; Lee, J. W.; Choi, D.; Kang, C. Y.; Kim, S. W.; Wang, Z. L.; Baik, J. M. Boosted output performance of triboelectric nanogenerator via electric double layer effect. *Nat. Commun.* **2016**, *7*, 12985.
- [25] Bai, Y.; Xu, L.; Lin, S. Q.; Luo, J. J.; Qin, H. F.; Han, K.; Wang, Z. L. Charge pumping strategy for rotation and sliding type triboelectric nanogenerators. *Adv. Energy Mater.* **2020**, *10*, 2000605.
- [26] Prada, T.; Harnchana, V.; Lakhonchai, A.; Chingsungnoen, A.; Poolcharuansin, P.; Chanlek, N.; Klamchuen, A.; Thongbai, P.; Amornkitbamrung, V. Enhancement of output power density in a modified polytetrafluoroethylene surface using a sequential O₂/Ar plasma etching for triboelectric nanogenerator applications. *Nano Res.*, in press, DOI: [10.1007/s12274-021-3470-4](https://doi.org/10.1007/s12274-021-3470-4).
- [27] Yu, J. B.; Hou, X. J.; Cui, M.; Shi, S. Z.; He, J.; Sun, Y. W.; Wang, C.; Chou, X. J. Flexible PDMS-based triboelectric nanogenerator for instantaneous force sensing and human joint movement monitoring. *Sci. China Mater.* **2019**, *62*, 1423–1432.
- [28] Liu, L.; Shi, Q. F.; Lee, C. A hybridized electromagnetic-triboelectric nanogenerator designed for scavenging biomechanical energy in human balance control. *Nano Res.*, in press, DOI: [10.1007/s12274-021-3540-7](https://doi.org/10.1007/s12274-021-3540-7).
- [29] Xu, L.; Bu, T. Z.; Yang, X. D.; Zhang, C.; Wang, Z. L. Ultrahigh charge density realized by charge pumping at ambient conditions for triboelectric nanogenerators. *Nano Energy* **2018**, *49*, 625–633.
- [30] Wang, J.; Wu, C. S.; Dai, Y. J.; Zhao, Z. H.; Wang, A.; Zhang, T. J.; Wang, Z. L. Achieving ultrahigh triboelectric charge density for efficient energy harvesting. *Nat. Commun.* **2017**, *8*, 88.
- [31] Shen, J. L.; Li, Z. L.; Yu, J. Y.; Ding, B. Humidity-resisting triboelectric nanogenerator for high performance biomechanical energy harvesting. *Nano Energy* **2017**, *40*, 282–288.
- [32] Yi, F.; Wang, X. F.; Niu, S. M.; Li, S. M.; Yin, Y. J.; Dai, K. R.; Zhang, G. J.; Lin, L.; Wen, Z.; Guo, H. Y. et al. A highly shape-adaptive, stretchable design based on conductive liquid for energy harvesting and self-powered biomechanical monitoring. *Sci. Adv.* **2016**, *2*, e1501624.
- [33] Zhang, N.; Qin, C.; Feng, T. X.; Li, J.; Yang, Z. R.; Sun, X. P.; Liang, E. J.; Mao, Y. C.; Wang, X. D. Non-contact cylindrical rotating triboelectric nanogenerator for harvesting kinetic energy from hydraulics. *Nano Res.* **2020**, *13*, 1903–1907.
- [34] Pu, X.; Liu, M. M.; Chen, X. Y.; Sun, J. M.; Du, C. H.; Zhang, Y.; Zhai, J. Y.; Hu, W. G.; Wang, Z. L. Ultrastretchable, transparent triboelectric nanogenerator as electronic skin for biomechanical energy harvesting and tactile sensing. *Sci. Adv.* **2017**, *3*, e1700015.
- [35] Guan, Q. B.; Lin, G. H.; Gong, Y. Z.; Wang, J. F.; Tan, W. Y.; Bao, D. Q.; Liu, Y. N.; You, Z. W.; Sun, X. H.; Wen, Z. et al. Highly efficient self-healable and dual responsive hydrogel-based deformable triboelectric nanogenerators for wearable electronics. *J. Mater. Chem. A* **2019**, *7*, 13948–13955.
- [36] Yang, Y. Q.; Sun, N.; Wen, Z.; Cheng, P.; Zheng, H. C.; Shao, H. Y.; Xia, Y. J.; Chen, C.; Lan, H. W.; Xie, X. K. et al. Liquid-metal-based super-stretchable and structure-designable triboelectric nanogenerator for wearable electronics. *ACS Nano* **2018**, *12*, 2027–2034.
- [37] Wang, S.; Ding, L.; Fan, X. W.; Jiang, W. Q.; Gong, X. L. A liquid metal-based triboelectric nanogenerator as stretchable electronics for safeguarding and self-powered mechanosensing. *Nano Energy* **2018**, *53*, 863–870.
- [38] Fan, Y. J.; Meng, X. S.; Li, H. Y.; Kuang, S. Y.; Zhang, L.; Wu, Y.; Wang, Z. L.; Zhu, G. Stretchable porous carbon nanotube-elastomer hybrid nanocomposite for harvesting mechanical energy. *Adv. Mater.* **2017**, *29*, 1603115.
- [39] Matsunaga, M.; Hirofumi, J.; Kishimoto, S.; Ohno, Y. High-output, transparent, stretchable triboelectric nanogenerator based on carbon nanotube thin film toward wearable energy harvesters. *Nano Energy* **2020**, *67*, 104297.
- [40] Hwang, B. U.; Lee, J. H.; Trung, T. Q.; Roh, E.; Kim, D. I.; Kim, S. W.; Lee, N. E. Transparent stretchable self-powered patchable sensor platform with ultrasensitive recognition of human activities. *ACS Nano* **2015**, *9*, 8801–8810.
- [41] Wen, Z.; Yang, Y. Q.; Sun, N.; Li, G. F.; Liu, Y. N.; Chen, C.; Shi, J. H.; Xie, L. J.; Jiang, H. X.; Bao, D. Q. et al. A wrinkled PEDOT:PSS film based stretchable and transparent triboelectric nanogenerator for wearable energy harvesters and active motion sensors. *Adv. Funct. Mater.* **2018**, *28*, 1803684.
- [42] Qin, Z.; Yin, Y. Y.; Zhang, W. Z.; Li, C. J.; Pan, K. Wearable and stretchable triboelectric nanogenerator based on crumpled nanofibrous membranes. *ACS Appl. Mater. Interfaces* **2019**, *11*, 12452–12459.
- [43] Yang, P. K.; Lin, L.; Yi, F.; Li, X. H.; Pradel, K. C.; Zi, Y. L.; Wu, C. I.; He, J. H.; Zhang, Y.; Wang, Z. L. A flexible, stretchable and shape-adaptive approach for versatile energy conversion and self-powered biomedical monitoring. *Adv. Mater.* **2015**, *27*, 3817–3824.
- [44] Kwak, S. S.; Kim, H.; Seung, W.; Kim, J.; Hinchet, R.; Kim, S. W. Fully stretchable textile triboelectric nanogenerator with knitted fabric structures. *ACS Nano* **2017**, *11*, 10733–10741.
- [45] Chen, C. Y.; Chen, L. J.; Wu, Z. Y.; Guo, H. Y.; Yu, W. D.; Du, Z. Q.; Wang, Z. L. 3D double-faced interlock fabric triboelectric nanogenerator for bio-motion energy harvesting and as self-powered stretching and 3D tactile sensors. *Mater. Today* **2020**, *32*, 84–93.
- [46] Wei, Z. H.; Yan, K. Y.; Chen, H. N.; Yi, Y.; Zhang, T.; Long, X.; Li, J. K.; Zhang, L. X.; Wang, J. N.; Yang, S. H. Cost-efficient clamping solar cells using candle soot for hole extraction from ambipolar perovskites. *Energy Environ. Sci.* **2014**, *7*, 3326–3333.
- [47] Chen, H. M.; Xu, Y.; Zhang, J. S.; Wu, W. T.; Song, G. F. Theoretical system of contact-mode triboelectric nanogenerators for high energy conversion efficiency. *Nanoscale Res. Lett.* **2018**, *13*, 346.
- [48] Li, H. C.; Xu, Y.; Li, X. M.; Chen, Y.; Jiang, Y.; Zhang, C. X.; Lu, B. W.; Wang, J.; Ma, Y. J.; Chen, Y. H. et al. Epidermal Inorganic Optoelectronics for Blood Oxygen Measurement. *Adv. Healthc. Mater.* **2017**, *6*, 1601013.